CCD Photometry, Light Curve Modeling, and Period Study of GSC 2624-0941, a Totally Eclipsing Overcontact Binary System

Kevin B. Alton
UnderOak Observatory, 70 Summit Avenue, Cedar Knolls, NJ 07927; kbalton@optonline.net

John C. Downing
La Ventana Observatory, 28881 Sunset Road, Valley Center, CA 92082; johndowning2014@outlook.com

Received Septemver 4, 2021; revised October 26, November 3, 2021; accepted November 3, 2021

Abstract Precise time-series multi-color (BVR_c or I_c) light curve (LC) data were acquired from GSC 2624-0941 (= NSVS 8114939 = 2MASS J18275502+3148337) at three different sites between 2018 and 2021. New times of minimum (ToM) from data acquired during this study along with other ToMs extrapolated from the SuperWASP survey were used to generate an updated linear ephemeris. Secular analyses (ToM differences vs. epoch) revealed changes in the orbital period of GSC 2624-0941 over the past 17 years suggesting an apparent increase in the orbital period based on a parabolic fit of the residuals. Simultaneous modeling of multi-color LC data was accomplished using the Wilson-Devinney code. Since a total eclipse is observed, a photometrically derived value for the mass ratio (q_{ptm}) with acceptable uncertainty could be determined which subsequently provided estimates for some physical and geometric elements of GSC 2624-0941.

1. Introduction

Sparsely sampled monochromatic photometric data from GSC 2624-0941 (= NSVS 8114839 = 2MASS J18275502+3148337) were first captured during the ROTSE-I survey between 1999 and 2000 (Akerlof *et al.* 2000; Wozniak *et al.* 2004). Gettel *et al.* (2006) included GSC 2624-0941 in their catalog of bright contact binary stars from the ROTSE-I survey. Other sources of photometric data from this variable system include the All-Sky Automated Survey for SuperNovae (ASAS-SN) (Shappee *et al.* 2014; Jayasinghe *et al.* 2018) and the SuperWASP Survey (Butters *et al.* 2010). Herein, the first multi-color (BVI_c) LCs from GSC 2624-0941 with modeling using the Wilson-Devinney code (WD; Wilson and Devinney 1971; Wilson 1979, 1990) are reported. This investigation also includes secular analyses of the predicted vs. observed ToM differences (ETD) over the past 17 years.

2. Observations and data reduction

The imaging system used at UnderOak Observatory (UO, USA; 40.825 N, 74.456 W) during 2018 includes a 0.28-m Schmidt-Cassegrain telescope with an SBIG ST-8XME CCD camera. The focal-reduced (f/6.4) optics for this telescope produce an image scale of 2.06 arcsec/pixel (bin = 2 × 2) and a field-of-view (FOV) of 26.4 × 17.6 arcmin. Additional time-series photometric observations were acquired in 2020 at Desert Blooms Observatory (DBO, USA; 31.941 N, 110.257 W) using a QSI 683 wsg-8 CCD camera mounted at the Cassegrain focus of a 0.4-m Schmidt-Cassegrain telescope. This focal-reduced (f/7.2) instrument produces an image scale of 0.76 arcsec/pixel (bin = 2 × 2) and a field-of-view (FOV) of 15.9 × 21.1 arcmin. The equipment at La Ventana Observatory (LVO, USA; 33.2418 N, 116.9781 W) included an iOptron CEM60 mount with an SBIG Aluma CCD694 camera installed at the Cassegrain focus of a 0.235-m Schmidt-Cassegrain telescope. TheSkyX Pro Edition 10.5.0 controlled the main (30-s exposures) and integrated guide cameras during image acquisition (science, darks, and flats). This focal-reduced (f/7) instrument produces an image scale of 1.14 arcsec/pixel (bin = 2 × 2) and a field-of-view (FOV) of 26.1 × 20.9 arcmin.

All three CCD cameras were equipped with photometric B, V, R_c, and/or I_c filters manufactured to match the Johnson-Cousins Bessell specification. Each site used the same image (science, darks, and flats) acquisition software (TheSkyX Pro Edition 10.5.0; Software Bisque 2019) which controlled the main and integrated guide cameras. Computer time was updated immediately prior to each session. Dark subtraction, flat correction, and registration of all images collected at DBO and LVO were performed with AIP4Win v2.4.0 (Berry and Burnell 2005). Instrumental readings from GSC 2624-0941 were reduced to catalog-based magnitudes using APASS DR9 values (Henden *et al.* 2009, 2010, 2011; Smith *et al.* 2011) built into MPO Canopus v 10.7.1.3 (Minor Planet Observer 2010). Since data acquired in 2018 at UO (BVI_c) and in 2021 at LVO (BVR_c) did not produce total LC coverage, they were only used to supplement ToM values for secular analyses.

LCs were generated using an ensemble of five comparison stars, the average of which remained constant (< ±0.01 mag) throughout every imaging session. The identity, J2000 coordinates, and color indices (B–V) for these stars are provided in Table 1. A CCD image annotated with the location of the target (T) and comparison stars (1–5) is shown in Figure 1. Data acquired below 30° altitude (airmass > 2.0) were excluded; considering the close proximity of all program stars, differential atmospheric extinction was ignored. All photometric data acquired at DBO, LVO, and UO can be retrieved from the AAVSO International Database (Kafka 2021).

3. Results and discussion

Results and detailed discussion about the determination of linear and quadratic ephemerides follow below. Thereafter, discussion about our multi-source approach for estimating

Table 1. Astrometric coordinates (J2000), V-magnitudes and color indices (B–V) for GSC 2624-0941 (Figure 1), and the corresponding comparison stars used in this photometric study.

Star Identification	*R.A. (J2000)*[a] *h m s*	*Dec. (J2000)*[a] *° ′ ″*	*V-mag.*[b]	*(B–V)*[b]
(1) GSC 2624-2493	18 28 38.6037	+31 48 40.788	11.561	0.286
(2) GSC 2628-0523	18 28 50.8935	+31 53 01.478	11.738	0.551
(3) GSC 2628-0540	18 28 44.3862	+31 54 36.613	11.942	0.344
(4) GSC 2628-2268	18 28 34.4246	+31 54 03.090	13.389	0.434
(5) GSC 2628-2281	18 27 46.3159	+31 54 26.466	11.172	0.657
(T) GSC 2624-0941	18 27 55.0365	+31 48 33.798	11.953	0.350

a. R.A. and Dec. from Gaia DR2 (Gaia Collab. et al. *2016, 2018).*
b. V-magnitude and (B–V) for comparison stars derived from APASS DR9 database described by Henden et al. *2009, 2010, 2011, and Smith* et al. *2011.*

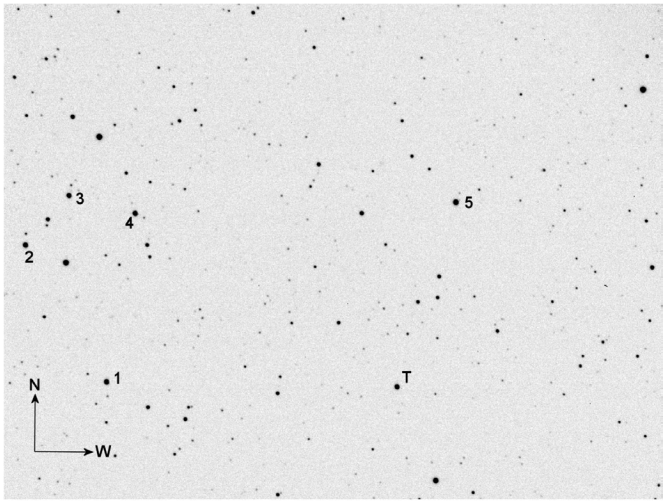

Figure 1. CCD image (V mag; 45 s) of GSC 2624-0941 (T) acquired at DBO (FOV = 15.9 × 21.1 arcmin) showing the location of comparison stars (1–5) used to generate APASS DR9-derived magnitude estimates.

T_{eff} and Roche-lobe modeling results with the WD code are examined. Finally, preliminary estimates for mass ($M_{\odot}$) and radius ($R_{\odot}$) along with corresponding calculations for luminosity ($L_{\odot}$), surface gravity (log (g)), semi-major axis ($R_{\odot}$), and bolometric magnitude (M_{bol}) are derived.

3.1. Photometry and ephemerides

Times of minimum (ToM) and associated errors were calculated according to Andrych and Andronov (2019) and Andrych *et al.* (2020) using the program MAVKA (https://uavso.org.ua/mavka/). Around Min I, simulation of

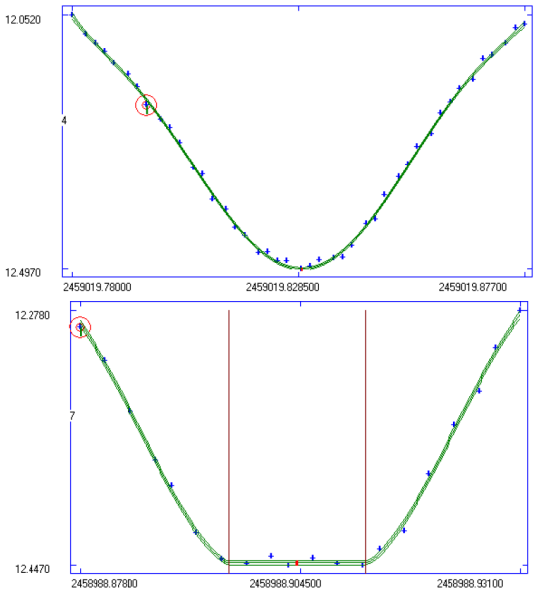

Figure 2. The top panel depicts time of minimum estimates during Min I using polynomial approximation (α = 6), while the bottom panel shows the fit achieved with the wall-supported line algorithm during Min II. In both cases, a circled red dot signifies the moment of extremum. The boundary lines which indicate the duration of the Min II total eclipse (0.016398 d) are conveniently calculated by MAVKA.

extrema was automatically optimized by finding the most precise degree (α) and best fit algebraic polynomial expression (Figure 2: top panel). During Min II, a "wall-supported line" (WSL) algorithm (Andrych *et al.* 2017) provided the best fit as the eclipse passes through totality resulting in a flattened bottom (Figure 2, bottom panel). These two, along with seven additional methods featured in MAVKA, are also well suited for other variable star LCs with symmetric or asymmetric extrema. ToM differences (ETD) vs. epoch were fit using scaled Levenberg-Marquardt algorithms (QtiPlot 0.9.9–rc9; IONDEV SRL 2021). Photometric uncertainty was calculated according to the so-called "CCD Equation" (Mortara and Fowler 1981; Howell 2006). The acquisition dates, number of data points, and uncertainty for each bandpass used for the determination of ToM values and/or WD modeling are summarized in Table 2.

Twelve new ToM measurements were extracted from photometric data acquired at DBO, LVO, and UO. The SuperWASP survey (Butters *et al.* 2010) provided an abundance of photometric data taken (30-s exposures) at modest cadence that repeats every 9 to 12 min. In some cases (n = 84) these data acquired between 2004 and 2008 were amenable to further

Table 2. Number of data points, estimated uncertainty (±, mag) in each bandpass (BVR_cI_c) and summary of image acquisition dates for GSC 2624-0941.

n (B)	*B (± mag.)*	*n (V)*	*V (± mag.)*	*n (R_c)*	*R_c (± mag.)*	*n (I_c)*	*I_c (± mag.)*	*Location*	*Dates*
351	0.008	355	0.006	—	—	347	0.005	UO	Aug. 6–Sept. 14, 2018
591	0.003	607	0.002	—	—	604	0.003	DBO	July 14–July 20, 2020
219	0.004	216	0.003	218	0.004	—	—	LVO	July 29–Aug. 2, 2021

Table 3. GSC~2624-0941 times-of-minimum (May 12, 2004-August 2, 2021), cycle number and residuals (ETD) between observed and predicted times derived from the updated linear ephemeris (Equation 1).

HJD 2400000+	*HJD Error*	*Cycle No.*	*ETD[a]*	*Reference*	*HJD 2400000+*	*HJD Error*	*Cycle No.*	*ETD[a]*	*Reference*
53137.6162	0.0003	–12714	0.0167	1	54320.4405	0.0002	–10323.5	0.0121	1
53138.6067	0.0003	–12712	0.0177	1	54321.4295	0.0002	–10321.5	0.0115	1
53139.5956	0.0004	–12710	0.0169	1	54322.4187	0.0002	–10319.5	0.0111	1
53141.5738	0.0005	–12706	0.0159	1	54324.3970	0.0005	–10315.5	0.0102	1
53155.6776	0.0004	–12677.5	0.0178	1	54593.5691	0.0004	–9771.5	0.0089	1
53157.6562	0.0003	–12673.5	0.0172	1	54609.6492	0.0004	–9739	0.0078	1
53158.6458	0.0004	–12671.5	0.0172	1	54613.6090	0.0004	–9731	0.0093	1
53162.6046	0.0004	–12663.5	0.0176	1	54618.5566	0.0003	–9721	0.0088	1
53165.5721	0.0003	–12657.5	0.0163	1	54619.5457	0.0002	–9719	0.0083	1
53166.5610	0.0002	–12655.5	0.0155	1	54619.5457	0.0002	–9719	0.0083	1
53167.5512	0.0002	–12653.5	0.0162	1	54620.5354	0.0003	–9717	0.0084	1
53168.5402	0.0002	–12651.5	0.0155	1	54620.5355	0.0003	–9717	0.0085	1
53173.4894	0.0002	–12641.5	0.0167	1	54621.5255	0.0003	–9715	0.0089	1
53177.6945	0.0002	–12633	0.0159	1	54622.5153	0.0004	–9713	0.0090	1
53178.4377	0.0003	–12631.5	0.0169	1	54622.5154	0.0003	–9713	0.0091	1
53179.6743	0.0003	–12629	0.0165	1	54624.4954	0.0003	–9709	0.0099	1
53180.6636	0.0003	–12627	0.0162	1	54625.4840	0.0002	–9707	0.0089	1
53182.6431	0.0003	–12623	0.0165	1	54626.4734	0.0002	–9705	0.0087	1
53183.6324	0.0002	–12621	0.0162	1	54640.5754	0.0004	–9676.5	0.0088	1
53183.6324	0.0002	–12621	0.0162	1	54641.5654	0.0003	–9674.5	0.0092	1
53184.6220	0.0003	–12619	0.0162	1	54650.4715	0.0002	–9656.5	0.0088	1
53185.6122	0.0005	–12617	0.0167	1	54652.4505	0.0002	–9652.5	0.0086	1
53192.5391	0.0004	–12603	0.0164	1	54655.4197	0.0003	–9646.5	0.0090	1
53194.5176	0.0003	–12599	0.0157	1	54660.6147	0.0003	–9636	0.0085	1
53195.5073	0.0003	–12597	0.0158	1	54660.6147	0.0003	–9636	0.0085	1
53196.4963	0.0003	–12595	0.0152	1	54661.6047	0.0005	–9634	0.0089	1
53197.4865	0.0002	–12593	0.0158	1	54663.5846	0.0005	–9630	0.0096	1
53198.4760	0.0004	–12591	0.0156	1	54665.5645	0.0005	–9626	0.0103	1
53199.4658	0.0002	–12589	0.0159	1	54665.5653	0.0007	–9626	0.0111	1
53200.4551	0.0003	–12587	0.0155	1	54666.5540	0.0004	–9624	0.0102	1
53201.4456	0.0003	–12585	0.0164	1	54670.5112	0.0003	–9616	0.0090	1
53223.4641	0.0004	–12540.5	0.0162	1	54671.5011	0.0003	–9614	0.0092	1
53224.4534	0.0003	–12538.5	0.0159	1	54672.4894	0.0002	–9612	0.0079	1
53225.4436	0.0003	–12536.5	0.0164	1	54674.4688	0.0002	–9608	0.0081	1
53227.4218	0.0002	–12532.5	0.0155	1	54675.4585	0.0002	–9606	0.0082	1
53229.4009	0.0003	–12528.5	0.0153	1	54676.4478	0.0002	–9604	0.0080	1
53242.5145	0.0004	–12502	0.0166	1	58354.5658	0.0001	–2170.5	0.0004	2
53243.5044	0.0004	–12500	0.0169	1	58355.5549	0.0001	–2168.5	–0.0001	2
53249.4417	0.0007	–12488	0.0166	1	58366.6879	0.0002	–2146	–0.0002	2
53252.4099	0.0002	–12482	0.0159	1	58988.9042	0.0002	–888.5	0.0001	2
53253.4007	0.0002	–12480	0.0172	1	58990.8831	0.0008	–884.5	–0.0003	2
54296.4409	0.0003	–10372	0.0105	1	59015.8712	0.0003	–834	0.0003	2
54297.4312	0.0003	–10370	0.0112	1	59017.8505	0.0002	–830	0.0003	2
54298.4206	0.0003	–10368	0.0109	1	59019.8289	0.0001	–826	–0.0004	2
54307.5730	0.0005	–10349.5	0.0095	1	59021.8083	0.0001	–822	–0.0003	2
54316.4814	0.0004	–10331.5	0.0114	1	59031.7045	0.0001	–802	–0.0001	2
54318.4604	0.0003	–10327.5	0.0113	1	59424.8262	0.0001	–7.5	–0.0002	2
54318.4604	0.0003	–10327.5	0.0113	1	59428.7853	0.0001	0.5	0.0004	2
54318.4607	0.0003	–10327.5	0.0115	1					

a. ETD = Eclipse Time Difference. b. nr = not reported. References: 1. SuperWASP (Butters et al. *2010); 2. This study.*

analysis using MAVKA (Andrych and Andronov 2019; Andrych *et al.* 2020) to estimate ToM values. All available ToM values are provided in Table 3. A new linear ephemeris based on results obtained between 2018 and 2021 was determined as follows:

$$\text{Min. I (HJD)} = 2459428.5375\,(2) + 0.4948040\,(1)\,\text{E} \ . \quad (1)$$

Plotting (Figure 3) the difference (ETD) between observed eclipse times and those predicted by the linear ephemeris against epoch (cycle number) reveals what appears to be a quadratic relationship (Equation 2) where:

$$\text{ETD} = 7.08 \pm 23.97 \cdot 10^{-5} + 2.6021 \pm 0.7704 \cdot 10^{-7}\ \text{E} \\ 1.2307 \pm 0.0548 \cdot 10^{-10}\ \text{E}^2 \ . \quad (2)$$

Given that the coefficient of the quadratic term (Q) is positive, this result would suggest that the orbital period has been increasing at the rate ($dP/dt = 2Q/P$) of $0.0157 \pm 0.0007\ \text{s} \cdot \text{y}^{-1}$. The absolute rate is similar to many other overcontact systems reported in the literature (Latković *et al.* 2021). Secular period change described by a parabolic expression is often attributed to mass transfer or by angular momentum loss (AML) due to magnetic stellar wind (Qian 2001, 2003; Li *et al.* 2019).

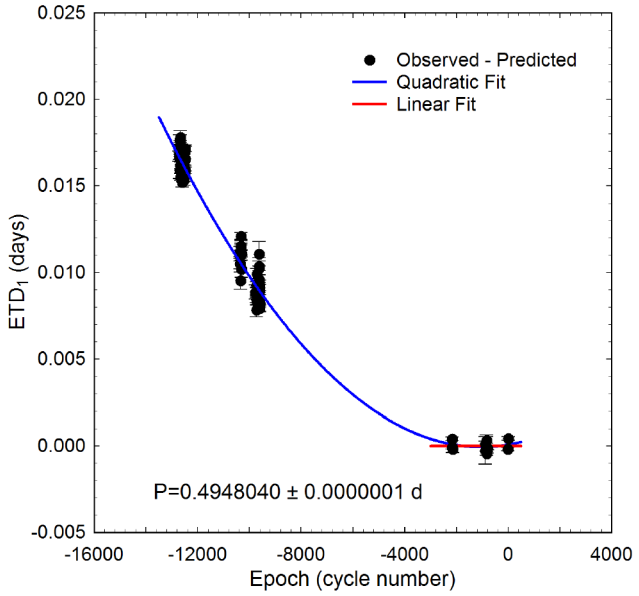

Figure 3. Linear and quadratic fits of ToM differences (ETD) vs. epoch for GSC 2624-0941 calculated using the new linear ephemeris (Equation 1). Measurement uncertainty is denoted by the error bars.

Table 4. Estimation of effective temperature (T_{eff1}) of the primary star in GSC 2624-0941.

Parameter	*Value*
DBO $(B–V)_0$	0.268 ± 0.021
Median combined $(B–V)_0$[a]	0.269 ± 0.023
Galactic reddening E(B–V)[b]	0.0809 ± 0.0032
Survey T_{eff1}[c](K)	7350 ± 160
Gaia T_{eff1}[d](K)	6925^{+625}_{-488}
Houdashelt T_{eff1}[e](K)	7107 ± 170
Median T_{eff1}(K)	7127 ± 190
Spectral Class[f]	A0V-F9V

a. Surveys and DBO intrinsic $(B–V)_0$ determined using reddening values (E (B–V)).
b. NASA/IPAC Infrared Science Archive (2021) (https://irsa.ipac.caltech.edu/applications/DUST/).
c. T_{eff1} interpolated from median combined $(B–V)_0$ using Table4 in Pecaut and Mamajek (2013).
d. Values from Gaia DR2 (Gaia Collab. 2016, 2018) (http://vizier.u-strasbg.fr/viz-bin/VizieR?-source=I/345/gaia2).
e. Values calculated with Houdashelt et al. *(2000) empirical relationship*
f. Spectral class estimated from Pecaut and Mamajek (2013).

Ideally when AML dominates, the net effect is a decreasing orbital period. If conservative mass transfer from the most massive to a less massive secondary star prevails, then the orbital period can also speed up. Separation increases when conservative mass transfer from the less massive to a more massive component takes place or spherically symmetric mass loss from either body (e.g. a wind but not magnetized) occurs. In mixed situations (e.g. mass transfer from less massive star, together with AML) the orbit evolution depends on which process dominates.

3.2. Effective temperature estimation

The effective temperature (T_{eff1}) of the more massive, and therefore most luminous component (defined as the primary

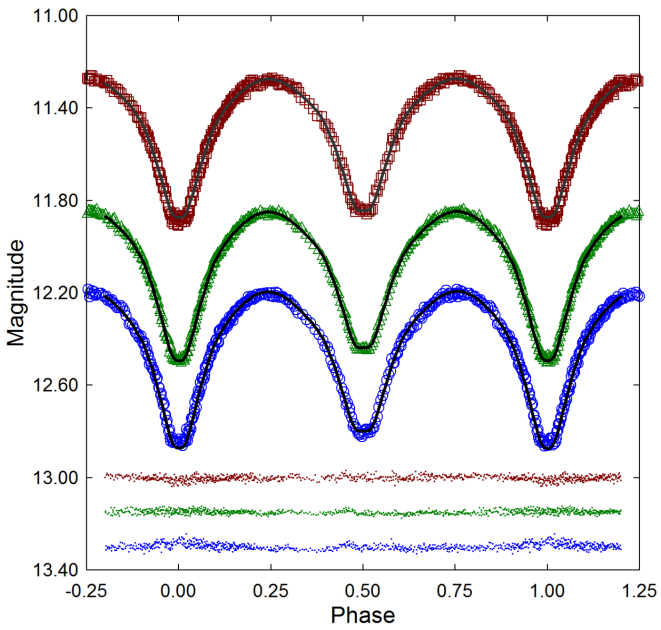

Figure 4. Period-folded (0.4948025 ± 0.0000001 d) CCD-derived LCs for GSC 2624-0941 produced from photometric data collected at DBO between July 14, 2020, and July 20, 2020. The top (I_c), middle (V), and bottom curves (B) were transformed to magnitudes based on APASS DR9-derived catalog values from comparison stars. In this case, the model assumed an A-subtype overcontact binary with single spot on the primary star; residuals from the model fits are offset at the bottom of the plot to keep the values on scale.

Table 5. Light curve parameters evaluated by WD modeling and the geometric elements derived for GSC 2624-0941 (2020) assuming it is an A-type W UMa variable.

Parameter[a]	*DBO No Spot*	*DBO Spotted*
T_{eff1} (K)[b]	7127 (190)	7127 (190)
T_{eff2} (K)	7065(188)	6939 (185)
q (m_2/m_1)	0.396 (1)	0.417 (3)
A[b]	0.50	0.50
g[b]	0.32	0.32
$\Omega_1=\Omega_2$	2.622 (2)	2.663 (2)
Ω_{inner}	2.670 (2)	2.711 (4)
Ω_{outer}	2.428 (1)	2.458 (3)
i°	85.43 (3)	83.4 (1)
$A_P=T_S/T_{star}$[c]	—	0.80 (1)
Θ_P (spot co-latitude)[c]	—	80 (2)
φ_P (spot longitude)[c]	—	189 (1)
r_P (angular radius)[c]	—	12 (1)
$L_1/(L_1+L_2)B$[d]	0.7033 (2)	0.7089 (1)
$L_1/(L_1+L_2)V$	0.7020 (1)	0.7051 (1)
$L_1/(L_1+L_2)I_c$	0.7006 (2)	0.7010 (1)
r_1 (pole)	0.4426 (3)	0.4384 (2)
r_1 (side)	0.4748 (4)	0.4696 (2)
r_1 (back)	0.5050 (4)	0.5002 (3)
r_2 (pole)	0.2914 (9)	0.2951 (7)
r_2 (side)	0.3052 (11)	0.3091 (8)
r_2 (back)	0.3452 (19)	0.3487 (15)
Fill-out factor (%)	19.8 (1.1)	19.0 (1.5)
RMS (B)[e]	0.01067	0.00832
RMS (V)	0.00846	0.00595
RMS (I_c)	0.00919	0.00794

a. All DBO uncertainty estimates for T_{eff2}, q, $\Omega_{1,2}$, i, $r_{1,2}$, and L_1 from WDWINT56A (Nelson 2009). b. Fixed with no error during DC. c. Spot parameters in degrees (Θ_P, φ_P, and r_P) or A_P in fractional degrees (K). d. L_1 and L_2 refer to scaled luminosities of the primary and secondary stars, respectively. e. Monochromatic residual mean square error from observed values.

star herein) was derived from a composite of photometric (2MASS and APASS) determinations that were as necessary transformed to (B–V) (http://www.aerith.net/astro/color_conversion.html; http://brucegary.net/dummies/method0.html). Interstellar extinction (A_V) and reddening ($E(B–V) = A_V / 3.1$) was estimated (image size = 2°) according to a galactic dust map model derived by Schlafly and Finkbeiner (2011). Additional sources used to establish a median value for each T_{eff1} included the Gaia DR2 release of stellar parameters (Andrae *et al.* 2018), and an empirical relationship (Houdashelt *et al.* 2000) based on intrinsic color. The median result ($T_{eff1} = 7127 \pm 190$ K), summarized in Table 4, was adopted for WD modeling of LCs from GSC 2624-0941.

3.3. Modeling approach with the Wilson-Devinney Code

Modeling of LC data from 2020 (Figure 4) was initially performed with PHOEBE 0.31a (Prša and Zwitter 2005) and then refined using WDwint56a (Nelson 2009). Both programs feature a graphical interface to the Wilson-Devinney WD2003 code (Wilson and Devinney 1971; Wilson 1979, 1990). WDwint56a incorporates Kurucz's atmosphere models (Kurucz 2002) that are integrated over BVI_c passbands. The final selected model was Mode 3 for an overcontact binary; other modes (detached and semi-detached) never achieved an improved LC simulation as defined by the model residual mean square error. Internal energy transfer to the stellar surface is driven by convective (7200 K) rather than radiative processes (Bradstreet and Steelman 2004). Therefore, bolometric albedo ($A_{1,2} = 0.5$) was assigned according to Ruciński (1969) while the gravity darkening coefficient ($g_{1,2} = 0.32$) was adopted from Lucy (1967). During model fit optimization with differential corrections (DC), logarithmic limb darkening coefficients (x_1, x_2, y_1, y_2) were interpolated (van Hamme 1993) following any change in the effective temperature. All but the temperature of the more massive star (T_{eff1}), $A_{1,2}$ and $g_{1,2}$ were allowed to vary during DC iterations. In general, the best fits for T_{eff2}, i, q and Roche potentials ($\Omega_1 = \Omega_2$) were collectively refined (method of multiple subsets) by DC using the multicolor LC data until a simultaneous solution was found. In this case, surface inhomogeneity often attributed to star spots was simulated by the addition of a cool spot on the primary star to obtain the best fit LC models around Min II. GSC 2624-0941 did not require third light correction ($l_3 = 0$) to improve WD model fits.

3.4. Wilson-Devinney modeling results

Without radial velocity (RV) data it is generally not possible to unambiguously determine the mass ratio or total mass of an eclipsing binary system. A total eclipse is observed at Min II, suggesting that GSC 2624-0941 is an A-subtype overcontact binary system (Binnendijk 1970). Like GSC 2624-0941, other A-type OCBs tend to have relatively hot (spectral class A-F) component stars and orbital periods between 0.4 and 0.8 d. Since the proposed T_{eff1} (7127 K) for the primary approached the generally regarded boundary (7200 K) between convective and radiative energy transfer, we attempted to model the LCs using gravity-brightening ($g_1 = 1$ and $g_{1,2} = 1$) and albedo ($A_1 = 1$ and $A_{1,2} = 1$) values associated with a radiative star. These changes always produced inferior LC fits compared to those obtained when assuming GSC 2624-0941 was a purely convective system ($g_{1,2} = 0.32$ and $A_{1,2} = 0.5$).

Standard errors reported in Table 5 are computed from the DC covariance matrix and only reflect the model fit to the observations which assume exact values for any fixed parameter. These formal errors are generally regarded as unrealistically small, considering the estimated uncertainties associated with the mean adopted T_{eff1} values along with basic assumptions about $A_{1,2}$, $g_{1,2}$ and the influence of spots added to the WD model. Normally, the value for T_{eff1} is fixed with no error during modeling with the WD code. When T_{eff1} is varied by as much as ±10%, investigations with other OCBs, including A- (Alton 2019; Alton *et al.* 2020) and W-subtypes (Alton and Nelson 2018), have shown that uncertainty estimates for i, q, or $\Omega_{1,2}$ were not appreciably (<2.5%) affected. Assuming that the actual T_{eff1} value falls within ±10% of the adopted values used for WD modeling (a reasonable expectation based on T_{eff1} data provided in Table 4), then uncertainty estimates for i, q, or $\Omega_{1,2}$ along with spot size, temperature, and location would likely not exceed this amount.

The fill-out parameter (f) which corresponds to the outer surface shared by each star was calculated according to Equation 2 (Kallrath and Milone 2009; Bradstreet 2005) where:

$$f = (\Omega_{inner} - \Omega_{1,2}) / (\Omega_{inner} - \Omega_{outer}) , \quad (3)$$

wherein Ω_{outer} is the outer critical Roche equipotential, Ω_{inner} is the value for the inner critical Roche equipotential, and $\Omega = \Omega_{1,2}$ denotes the common envelope surface potential for the binary system. In this case GSC 2624-0941 is considered overcontact since $0 < f < 1$.

Spatial renderings (Figure 5) were produced with Binary Maker 3 (BM3; Bradstreet and Steelman 2004) using the final WDWint56a modeling results from 2020. The smaller secondary is shown to completely transit across the primary face during the deepest minimum ($\varphi = 0.0$), thereby confirming that the secondary star is totally eclipsed at Min II.

3.5. Preliminary stellar parameters

Mean physical characteristics were estimated for GSC 2624-0941 (Table 6) using results from the best fit (spotted) LC simulations from 2020. It is important to note that without the benefit of RV data which define the orbital motion, mass ratio, and total mass of the binary pair, these results should be considered "relative" rather than "absolute" parameters and regarded as preliminary. Nonetheless, since the photometric mass ratio (q_{ptm}) is derived from a totally eclipsing OCB, there is a reasonable expectation that DC optimization with the WD2003 code would have arrived at a solution with acceptable uncertainty for q (Terrell and Wilson 2005).

Calculations are described below for estimating the solar mass and size, semi-major axis, solar luminosity, bolometric V-mag, and surface gravity of each component. Three empirically derived mass-period relationships (M-PR) for W UMa-binaries were used to estimate the primary star mass. The first M-PR was reported by Qian (2003), while two others followed, from Gazeas and Stępień (2008) and then Gazeas (2009). According to Qian (2003), when the primary star is

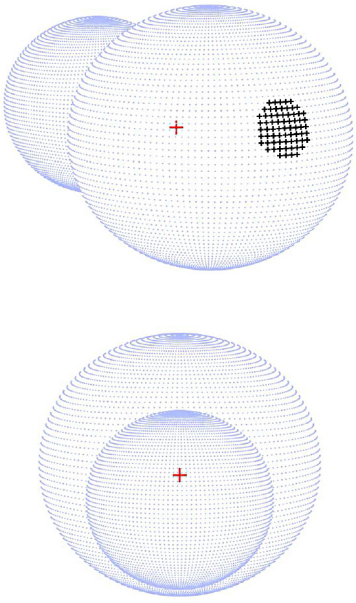

Figure 5. Three-dimensional spatial model of GSC 2624-0941 during 2020 illustrating (top) the location of a cool (black) spot on the primary star and (bottom) the secondary star transit across the primary star face at Min I (φ = 0.0).

greater than 1.35 $M_\odot$ or the system is A-type, its mass can be determined from:

$$M_1 = 0.761\,(150) + 1.82\,(28) \cdot P\,; \qquad (4)$$

where P is the orbital period in days and leads to $M_1 = 1.662 \pm 0.204\,M_\odot$ for the primary. The M-PR derived by Gazeas and Stępień (2008):

$$\log(M_1) = 0.755\,(59) \cdot \log(P) + 0.416\,(24)\,; \qquad (5)$$

corresponds to an OCB system where $M_1 = 1.532 \pm 0.106\ M_\odot$. Gazeas (2009) reported another empirical relationship for the more massive (M_1) star of a contact binary such that:

$$\log(M_1) = 0.725\,(59) \cdot \log(P) - 0.076\,(32) \cdot \log(q) + 0.365\,(32). \qquad (6)$$

from which $M_1 = 1.487 \pm 0.114\,M_\odot$. The median of three values ($M_1 = 1.532 \pm 0.045\,M_\odot$) estimated from Equations 4–6 was used for subsequent determinations of M_2, semi-major axis a, volume-radii r_L, and bolometric magnitudes (M_{bol}) using the formal errors calculated by WDWINT56A (Nelson 2009). The secondary mass = $0.638 \pm 0.019\,M_\odot$ and total mass ($2.170 \pm 0.049\,M_\odot$) were determined using the mean photometric mass ratio ($q_{ptm} = 0.417 \pm 0.003$) derived from the best fit (spotted) models.

The semi-major axis, $a(R_\odot) = 3.409 \pm 0.025$, was calculated from Newton's version of Kepler's third law where:

$$a^3 = (G \cdot P^2\,(M_1 + M_2)) / (4\pi^2). \qquad (7)$$

The effective radius of each Roche lobe (r_L) can be calculated over the entire range of mass ratios ($0 < q < \infty$) according to an expression derived by Eggleton (1983):

$$r_L = (0.49q^{2/3}) / (0.6q^{2/3} + \ln(1 + q^{1/3})), \qquad (8)$$

Table 6. Fundamental stellar parameters for GSC 2624-0941 using the photometric mass ratio ($q_{ptm} = m_2 / m_1$) from the spotted WD model fits of LC data (2020) and the estimated primary star mass based on empirically derived M-PRs for overcontact binary systems.

Parameter	*Primary*	*Secondary*
Mass ($M_\odot$)	1.532 ± 0.045	0.638 ± 0.019
Radius ($R_\odot$)	1.555 ± 0.012	1.044 ± 0.008
a ($R_\odot$)	3.409 ± 0.025	3.409 ± 0.025
Luminosity ($L_\odot$)	5.631 ± 0.606	2.276 ± 0.245
M_{bol}	2.873 ± 0.117	3.857 ± 0.117
Log (g)	4.240 ± 0.014	4.206 ± 0.014

from which values for r_1 (0.4562 ± 0.0002) and r_2 (0.3063 ± 0.0002) were determined for the primary and secondary stars, respectively. Since the semi-major axis and the volume radii are known, the radii in solar units for both binary components can be calculated where $R_1 = a \cdot r_1 = 1.555 \pm 0.012\,R_\odot$ and $R_2 = a \cdot r_2 = 1.044 \pm 0.008\,R_\odot$.

Luminosity in solar units ($L_\odot$) for the primary (L_1) and secondary stars (L_2) was calculated from the well-known relationship derived from the Stefan-Boltzmann law (Equation 9) where:

$$L_{1,2} = (R_{1,2}/R_\odot)^2\,(T_{1,2}/T_\odot)^4. \qquad (9)$$

Assuming that $T_{eff1} = 7127$ K, $T_{eff2} = 6939$ K, and $T_\odot = 5772$ K, then the solar luminosities ($L_\odot$) for the primary and secondary are $L_1 = 5.631 \pm 0.606$ and $L_2 = 2.276 \pm 0.245$, respectively.

4. Conclusions

This first detailed photometric investigation of GSC 2624-0941 has added valuable information to a ever growing list of OCBs that have been physically and geometrically characterized with a reliable mass ratio. Although we did not uncover anything strikingly remarkable about this system, the proposed effective temperature ($T_{eff1} = 7127 \pm 190$ K) of the primary star proved to be within the top 8% hottest in a catalog of 687 individually studied W UMa stars (Latković *et al.* 2021). LCs from this variable star exhibit a flattened bottom during Min II, a characteristic of a totally eclipsing A-subtype OCB. Twelve new times of minimum for GSC 2624-0941 based on multicolor CCD data were determined from LCs acquired at three different locations between 2018 and 2021. These, along with other values (n = 84) extrapolated from the SuperWASP survey (2004–2008), led to updated linear and quadratic ephemerides. Secular analyses suggested that the orbital period of GSC 2624-0941 is changing at a rate ($0.0157\,s \cdot y^{-1}$) consistent with other similarly classified OCBs. The photometric mass ratio ($q_{ptm} = 0.417 \pm 0.003$) determined by WD modeling is expected to correspond closely to a mass ratio derived from RV data. Nonetheless, spectroscopic studies (RV and high resolution classification spectra) will be required to unequivocally determine a total mass and spectral class for each system. Consequently, all parameter values and corresponding uncertainties reported herein should be considered preliminary.

5. Acknowledgements

This research has made use of the SIMBAD database operated at Centre de Données astronomiques de Strasbourg, France. In addition, the Northern Sky Variability Survey hosted by the Los Alamos National Laboratory (https://skydot.lanl.gov/nsvs/nsvs.php), the All-Sky Automated Survey for Supernovae (https://asas-sn.osu.edu/variables), and the AAVSO International Database were mined for essential information. This work also presents results from the European Space Agency (ESA) space mission Gaia. Gaia data are being processed by the Gaia Data Processing and Analysis Consortium (DPAC). Funding for the DPAC is provided by national institutions, in particular the institutions participating in the Gaia MultiLateral Agreement (MLA). The Gaia mission website is https://www.cosmos.esa.int/gaia. The Gaia archive website is https://archives.esac.esa.int/gaia. This paper makes use of data from the first public release of the WASP data as provided by the WASP consortium and services at the NASA Exoplanet Archive, which is operated by the California Institute of Technology, under contract with the National Aeronautics and Space Administration under the Exoplanet Exploration Program. Many thanks to the anonymous referee whose valuable commentary led to significant improvement of this paper.

References

Akerlof, C., *et al.* 2000, *Astron. J.*, **119**, 1901.
Alton, K. B. 2019, *J. Amer. Assoc. Var. Star Obs.*, **47**, 7.
Alton, K. B., and Nelson, R. H. 2018, *Mon. Not. Roy. Astron. Soc.*, **479**, 3197.
Alton, K. B., Nelson, R. H. and Stępień, K. 2020, *J. Astrophys. Astron.*, **41**, 26.
Andrae, R., *et al.* 2018, *Astron. Astrophys.*, **616**, A8.
Andrych, K. D., and Andronov, I. L. 2019, *Open Eur. J. Var. Star*s, **197**, 65.
Andrych, K. D., Andronov, I. L., and Chinarova, L. L. 2017, *Odessa Astron. Publ.*, **30**, 57.
Andrych, K. D., Andronov, I. L., and Chinarova, L. L. 2020, *J. Phys. Stud.*, **24**, 1902.
Berry, R., and Burnell, J. 2005, *The Handbook of Astronomical Image Processing*, 2nd ed., Willmann-Bell, Richmond, VA.
Binnendijk, L. 1970, *Vistas Astron.*, **12**, 217.
Bradstreet, D. H. 2005, in *The Society for Astronomical Sciences 24th Annual Symposium on Telescope Science*, Society for Astronomical Sciences, Rancho Cucamonga, CA, 23.
Bradstreet, D. H., and Steelman, D. P. 2004, Binary Maker 3, Contact Software (http://www.binarymaker.com).
Butters, O. W., *et al.* 2010, *Astron. Astrophys.*, **520**, L10.
Eggleton, P. P. 1983, *Astrophys. J.*, **268**, 368.
Gaia Collaboration, *et al.* 2016, *Astron. Astrophys.*, **595A**, 1.
Gaia Collaboration, *et al.* 2018, *Astron. Astrophys.*, **616A**, 1.
Gazeas, K. D. 2009, *Commun. Asteroseismology*, **159**, 129.
Gazeas, K., and Stępień, K. 2008, *Mon. Not. Roy. Astron. Soc*., **390**, 1577.
Gettel, S. J., Geske, M. T., and McKay, T. A. 2006, *Astron. J.*, **131**, 621.
Henden, A. A., Levine, S. E., Terrell, D., Smith, T. C., and Welch, D. L., 2011, *Bull. Amer. Astron. Soc.*, **43**, 2011.
Henden, A. A., Terrell, D., Welch, D., and Smith, T. C. 2010, *Bull. Amer. Astron. Soc.*, **42**, 515.
Henden, A. A., Welch, D. L., Terrell, D., and Levine, S. E. 2009, *Bull. Amer. Astron. Soc.*, **41**, 669.
Houdashelt, M. L., Bell, R. A., and Sweigart, A. V. 2000, *Astron. J.*, **119**, 1448.
Howell, S. B. 2006, *Handbook of CCD Astronomy*, 2nd ed., Cambridge University Press, Cambridge.
Jayasinghe, T., *et al.* 2018, *Mon. Not. Roy. Astron. Soc.*, **477**, 3145.
Kafka, S. 2021, Observations from the AAVSO International Database (https://www.aavso.org/data-download).
Kallrath, J., and Milone, E. F. 2009, *Eclipsing Binary Stars: Modeling and Analysis*, Springer, New York.
Kurucz, R. L. 2002, *Baltic Astron.*, **11**, 101.
Latković, O., Čeki, A., and Lazarević, S. 2021, *Astrophys. J., Suppl. Ser.*, **254**, 10.
Li, K., *et al.* 2019, *Res. Astron. Astrophys.*, **19**, 147.
Lucy, L. B. 1967, *Z. Astrophys.*, **65**, 89.
Minor Planet Observer. 2010, MPO Software Suite (http://www.minorplanetobserver.com), BDW Publishing, Colorado Springs.
Mortara, L., and Fowler, A. 1981, in *Solid State Imagers for Astronomy*, SPIE Conf. Proc. 290, Society for Photo-Optical Instrumentation Engineers, Bellingham, WA, 28.
NASA/IPAC. 2021, NASA/IPAC Infrared Science Archive, Galactic Dust Reddening and Extinction (https://irsa.ipac.caltech.edu/applications/DUST/).
Nelson, R. H. 2009, WDwint56a: Astronomy Software by Bob Nelson (https://www.variablestarssouth.org/bob-nelson).
Pecaut, M. J., and Mamajek, E. E. 2013, *Astrophys. J., Suppl. Ser.*, **208**, 9.
Prša, A., and Zwitter, T. 2005, *Astrophys. J.*, **628**, 426.
Qian, S. 2001, *Mon. Not. Roy. Astron. Soc.*, **328**, 635.
Qian, S. 2003, *Mon. Not. Roy. Astron. Soc.*, **342**, 1260.
Ruciński, S. M. 1969, *Acta Astron.*, **19**, 245.
Schlafly, E. F., and Finkbeiner, D. P. 2011, *Astrophys. J.*, **737** 103.
Shappee, B. J., *et al.* 2014, *Astrophys. J.*, **788**, 48.
Smith, T. C., Henden, A. A., and Starkey, D. R. 2011, in *The Society for Astronomical Sciences 30th Annual Symposium on Telescope Science*, Society for Astronomical Sciences, Rancho Cucamonga, CA, 121.
Software Bisque. 2019, TheSkyX Professional Edition 10.5.0 (https://www.bisque.com).
Terrell, D., and Wilson, R. E. 2005, *Astrophys. Space Sci.*, **296**, 221.
van Hamme, W. 1993, *Astron. J.*, **106**, 2096.
Wilson, R. E. 1979, *Astrophys. J.*, **234**, 1054.
Wilson, R. E. 1990, *Astrophys. J.*, **356**, 613.
Wilson, R. E., and Devinney, E. J. 1971, *Astrophys. J.*, **166**, 605.
Woźniak, P. R., *et al.* 2004, *Astron. J.*, **127**, 2436.